Mater. Res. Soc. Symp. Proc. Vol. 1146 © 2009 Materials Research Society 1146-NN04-05

In-situ UHV TEM Investigation of the Reduction of Cu_2O Islands on Cu(100) Surfaces

Guangwen Zhou [1], Weiying Dai [2], Judith C. Yang [3]
[1] Department of Mechanical Engineering & Multidisciplinary Program in Materials Science and Engineering, State University of New York, Binghamton, NY 13902, U.S.A.
[2] MR Physics Center, Department of Radiology, Harvard University, Boston, MA 02215, U.S.A.
[3] Department of Mechanical Engineering and Materials Science, University of Pittsburgh, Pittsburgh, PA 15261, U.S.A.

ABSTRACT

In situ ultrahigh vacuum (UHV) transmission electron microscopy (TEM) is utilized to study the thermal reduction of Cu_2O nanoislands on Cu(100) surfaces. A linear decay behavior of the oxide islands is noted from *in situ* visualization of the oxide reduction. Complete reduction of the oxide islands leads to the formation of surface craters. Kinetic Monte Carlo (KMC) simulations are employed to elucidate the growth processes of the surface craters.

INTRODUCTION

The reduction of metal oxides plays critical roles in many fields including materials science, microelectronics, and chemical applications [1-3]. Traditionally, the reduction process has been described using phenomenological kinetic models, i.e., "nucleation and growth model" and "interface model". As shown in Fig. 1a, in the "nucleation and growth model", generation of small nuclei of the reduced phase occurs on the oxide surface and the reaction interface increases until growing nuclei coalesce and then decreases. In the "interface model", the rapid formation of a continuous layer of the reduced phase on the oxide surface occurs and the reaction boundary moves inward as the reaction proceeds (Fig 1b).

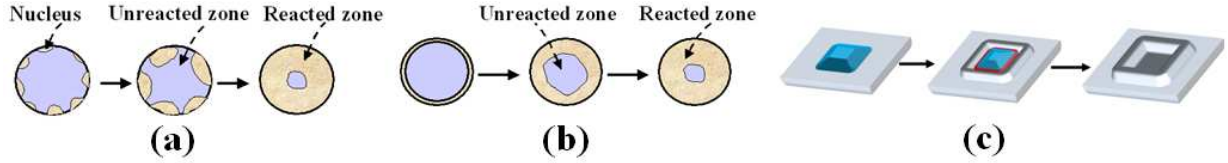

Figure 1: Comparison of the previously proposed oxide reduction models — (a) "nucleation and growth" model; (b) "interface" model — to (c) our proposed "perimeter" model for the reduction of oxide nanoislands on a metal surface, where the island perimeter is defined as the three-phase (metal-vacuum-oxide) contact line (marked by the red line), and oxide dissociation occurs preferentially at the island perimeter.

Although these kinetic models have been found useful in the description of the reduction of bulk oxides [4-6], here we show that they do not apply to the reduction of Cu_2O nanoislands on Cu surfaces. Our *in situ* TEM and AFM observations reveal that the reduction of these oxide islands results in the growth of the reduced phase (e.g., Cu) on the substrate surface surrounding the oxide islands rather than on the parent oxide; this is fundamentally different from the assumption by the phenomenological kinetic models. We show that the reduction of these surface oxide islands by this mechanism leads to the formation of surface craters (Fig. 1c).

EXPERIMENT

Our experiments were carried out in a modified JEOL 200CX TEM equipped to allow observation of oxidation and reduction under controlled gas environments [7]. The microscope was operated at 100 KeV to minimize possible irradiation effects. To avoid the possible electron beam induced oxide dissociation, the beam was on only when taking the images. Cu(100) single crystal films were grown on irradiated NaCl(100) by sputter deposition. The Cu films were removed from the substrate by floatation in de-ionized water, washed and mounted on a TEM specimen holder. Any native Cu oxide is removed *in situ* by annealing the films in the TEM under vacuum conditions at ~750°C, resulting in clean copper surfaces [8]. The *in situ* TEM experiments involve two steps: i) creation of Cu_2O islands on Cu(100) by *in situ* oxidation of Cu(100) surfaces inside the TEM, and ii) reduction of the Cu_2O islands by vacuum annealing. The first step has been discussed previously [9, 10]. After oxide islands grow to certain sizes during the oxidation, the oxygen gas leaking is then stopped and the microscope column is pumped to 8×10^{-8} torr quickly by attached UHV pumps. The reduction process is visualized *in situ* by annealing the oxidized Cu film under vacuum. Thereafter, the morphology of the reduced surfaces is analyzed by *ex situ* AFM.

RESULTS AND DISSCUSSION

The reduction of Cu_2O results in solid Cu and O_2 gas. The oxygen desorbs from the surface due to the small solubility of oxygen in copper [11]. Fig. 2a is a BF (bright field) TEM micrograph showing the morphology of the Cu film, where the oxide islands underwent initial reduction reaction for ~2 min at 800°C under vacuum. The occurrence of the dark contrast around the oxide islands is due to the formation of the reduced phase (Cu) layer on the substrate surface, as confirmed by selected area electron diffraction (SAD). Interestingly, the reduction of the oxide islands results in the growth of the reduced phase on the substrate surface around the oxide islands, rather than filling up the space left by the oxide. The growth of the reduced phase on the substrate surface also verifies that oxide reduction, instead of vaporization, occurred during the vacuum annealing. The 4-fold symmetry of the newly formed Cu overlayer is related to the (100) orientation of the Cu substrate. The newly formed Cu overlayer (e.g. the regions with dark contrast) and the adjacent bare Cu area give identical electron diffraction pattern (the inset in Fig. 2a), revealing the homoepitaxial growth of the Cu overlayer on the Cu(100) substrate. The contrast feature along the island perimeter (Fig. 2a) suggests that the island perimeter is the preferred site for the oxide decomposition.

The size evolution of the oxide islands under isothermal annealing can be followed inside the microscope. Fig. 2(b) is a sequential time series of *in situ* TEM images showing the size evolution of two oxide islands reduced at 750°C. The reduction of the islands results in the formation of new Cu layer on the substrate, causing the dark contrast around the islands. Fig. 2(c) is a plot of the island areas versus reduction time, and a linear decay behavior is noticed. In the following, we present a model based on the oxide dissociation along the island perimeter to explain the observed linear decay behavior of the oxide islands, where the perimeter of the oxide island is defined as the three-phase (metal-vacuum-oxide) contact line, as shown in Fig. 1(c).

The reduction process of the oxide islands is modeled as follows. The dissociation of Cu_2O along the island perimeter results in Cu atoms and oxygen, where the Cu atoms diffuse to

the substrate surface surrounding the oxide island. The Cu substrate provides a perfect template for the formation of the new Cu layer. The oxide dissociation along the island perimeter creates a shrinkage rate $dN(t)/dt = -CLJ$, where $N(t)$ is the total number of Cu atoms in a Cu_2O island at time t, C is the dissociation coefficient, J is the diffusive flux of copper atoms leaving the islands, and L is the island perimeter. The island lateral size is much larger than its thickness. By solving the above equation, it is found that the island cross-sectional area decreases linearly with respect to the reduction time, $A = A_0 - \frac{\Omega \pi JC}{\beta} t$, where Ω is the atomic volume of Cu in Cu_2O, β is the aspect ratio of the oxide island, A_0 is the cross-sectional area of the island before reduction reaction. The rate constant, $K=\Omega\pi JC/\beta$, depends on the island geometry, surface diffusion of Cu atoms, and oxide dissociation coefficient at the island perimeter. The solid lines in Fig. 2(c) are the theoretical fit to the experimental data, and the slope corresponds to the rate constant K. Since the two islands have similar shapes and undergo the same reduction condition, they have similar K, which can be discerned from the fitting in Fig. 2(c).

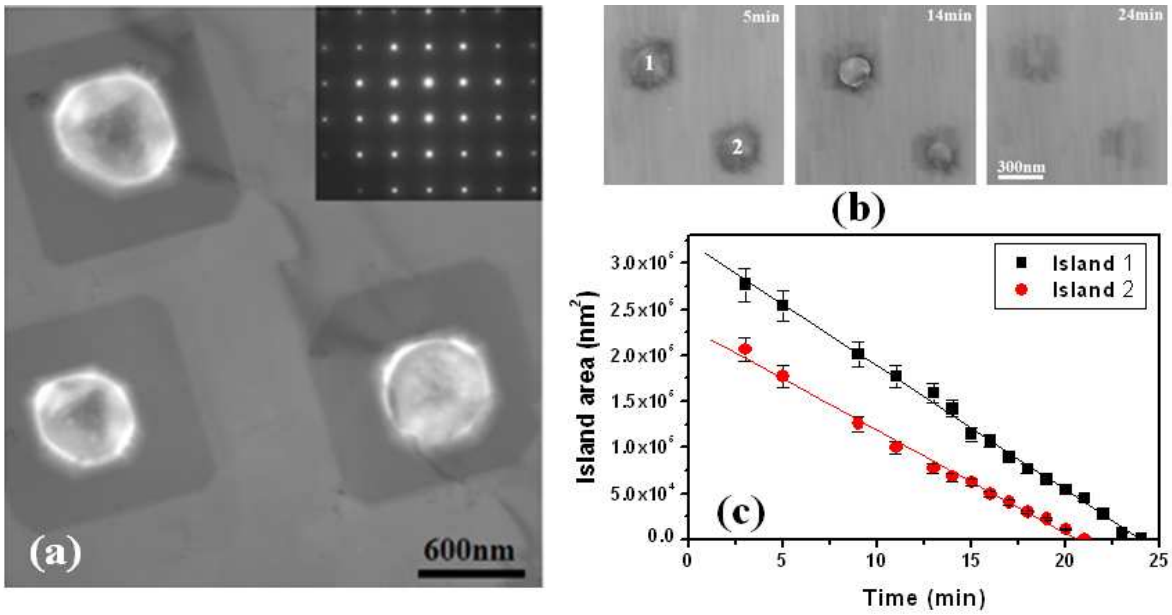

Figure 2: BF TEM image of Cu(100) after an initial reduction of the oxide islands at 800°C , the occurrence of dark contrast surrounding the reducing oxide islands is due to the homoepitaxial growth of new Cu overlayer, as revealed by the electron diffraction pattern (inset). The contrast feature along the island perimeter implies that the oxide decomposition occurs at the island perimeter; (b) *In situ* TEM observation of the reduction of two oxide islands at 750**°**C; (c) the cross-sectional area of the two oxide islands as a function of the reduction time, the solid lines correspond to the theoretical fit to the "perimeter model".

Cu(100) surfaces can be oxidized at different temperatures, leading to the formation of oxide islands with different morphologies [9, 10]. Fig. 3 shows AFM images of some oxide islands formed at different temperatures and the surface topology after the oxide islands are completely reduced. These AFM observations indicate that the reduction of the oxide islands results in the formation of surface craters and the craters take the shapes that are correlated with the original island shape. The rim height is roughly constant for each crater but varies among

different craters, ranging from 45nm to 70nm. Line-profile analysis of these craters reveals that the outer facets form angle α varying from 10° to 35° and the inner facets form angle β ranging from 20° to 60° with respect to the base plane along $[1\bar{1}0]$ direction, but α< β within the same crater. The definition of the contact angle of α and β is given in Fig. 4(a).

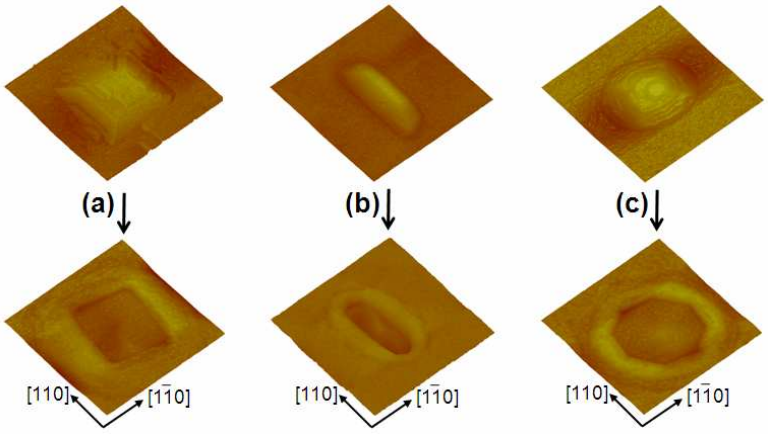

Figure 3: Representative AFM images of the oxide islands formed at different oxidation temperatures (a) 500°C, (b) 600°C, (c) 750°C, and the surface morphology of the Cu film after the reduction reaction at 800°C under vacuum (5×5μm^2, z range: 0.15μm).

One intriguing feature of these craters is the presence of tall crater rims. Unlike the three dimensional faceted structures in heteroepitaxial systems, the formation of the crater rims in the present homoepitaxial system cannot be attributed to epitaxial stress and should be kinetic in nature. The formation of large heights of the crater rims involves the transfer of Cu atoms dislodged from a reducing Cu_2O island to its adjacent growing crater rim. Since the oxide dissociation occurs at the island bottom, the homoepitaxial growth of the crater rim must call for upward adatom diffusion from the crater bottom onto the top of the growing rim. Such upward adatom diffusion is active whenever steps are present [12], and it becomes more efficient as increasing the substrate temperature (here T=800°C for the oxide reduction). Another striking feature of these craters is the asymmetrical slope evolution of the inner and outer facets of the crater rim. The inner facet angle β is steeper than the outer facet angle α for each crater, implying different kinetic processes along the inner and outer facets of the crater rim.

We use kinetic Monte Carlo simulations to gain a microscopic understanding of the homoepitaxial growth of the crater rim. The Cu homoepitaxy is initiated by the surface diffusion of Cu adatoms displaced from the reducing island. Surface migration of the adatoms is modeled as a nearest-neighbor hopping process at the rate, $k(E,T) = v_0 \exp(-E/k_BT)$, where E is the hopping barrier, T the substrate temperature, and k_B Boltzmann's constant. The attempt frequency v_0 is $v_0 = k_BT/h = 4.2\times10^{10}T$, with h Plank's constant, and T given in degrees Kelvin. The hopping barrier is composed of a substrate term E_S, a contribution E_N from each in-plane nearest neighbor, and the step-edge barrier E_B, i.e., $E=E_S+nE_N+(m_i-m_f)E_B$, where n is the number of in-plane nearest neighbor before the hop, m_i and m_f are the number of the next-nearest neighbors in the planes beneath and above the hopping atom before (m_i) and after (m_f) a hop, respectively [13]. The barrier E_B has a nonzero value only if $m_i>m_f$ and its effect is to make adatoms difficult to approach the step-edge sites [13]. If a site has two atoms as its nearest neighbors ((1+1)-

dimensional growth), then the adatom sticks and occupies this stable site. Otherwise, it will diffuse to one of the nearest sites. Notice that the presence of the step-edge barrier depends on a hop direction and the number of the next-nearest neighbors both before and after the hop has to be considered in order to detect a step. The model parameters used are E_S=0.49eV [14], E_N=0.24eV [14], and E_B=0.27eV [15], as obtained from the self-diffusion of Cu adatoms on terraces and at edges and steps.

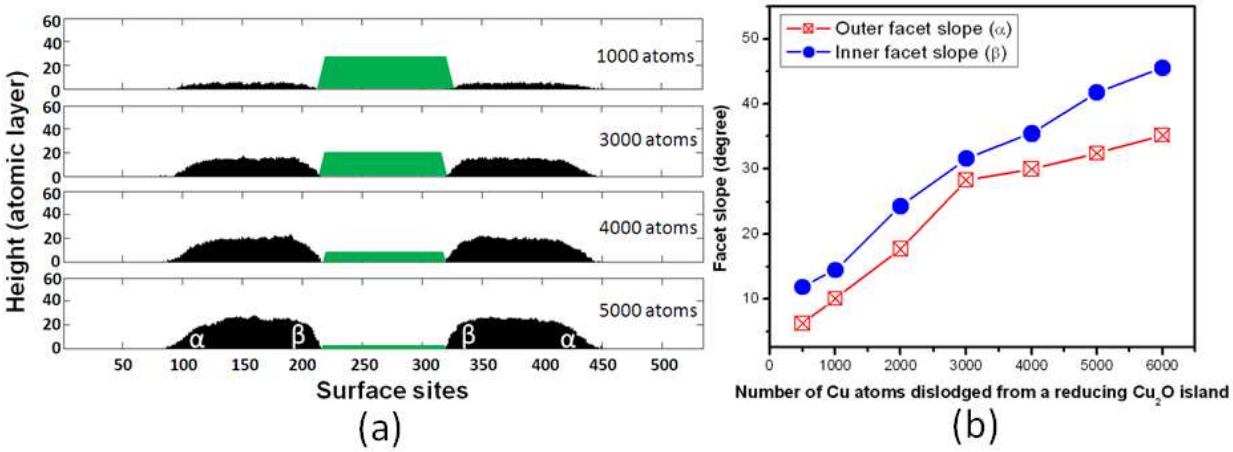

Figure 4: (a) KMC simulations of the crater formation via homoepitaxial growth of Cu at 800°C, α and β are the contact angle of the outer and inner facet with respect to the substrate. Reduction of the Cu_2O island is schematically shown at the center of the substrate as an eye guidance; (b) Slope evolution of the inner and outer facets of the rim observed from the KMC simulations.

The formation of the crater structure is observed from our (1+1)-dimensional KMC simulations. Fig. 4(a) shows a few snapshots of the morphological evolution of the crater from the simulations. Several distinct features can be identified from these simulations. First, both the inner and outer walls of the crater rim show the faceting instability, as illustrated by the thickness dependence of the facet contact angle with the substrate. The inner facet angle β is steeper than the outer facet angle α at each growth stage (i.e., α< β), as shown in Fig. 4(b). Both α and β are observed to grow, but exhibiting different growth behaviors. The simulations also reveal that there is a rapid increase in the rim height/width aspect ratio during the crater growth, which is consistent with experimental observation.

Homoepitaxy has conventionally been modeled as the processes of adatoms "raining" down onto a growing surface and pyramid-like mound morphologies are usually observed [16]. As deposition proceeds, the mounds grow bigger and steeper (i.e., unstable), and may ultimately reach a steady state characterized by an approximately constant mound angle due to the balance between an uphill current formed by the edge-step barrier [17-20] and a downhill current caused by the "downward funneling" effect [21, 22] or formation of some specific side facets that favor upward diffusion of adatoms [12, 15]. However, the growth of crater rims by the Cu homoepitaxy does not involve the deposition of adatoms onto the growing surface; alternatively, the adatoms are supplied from a confined Cu source at the crater center at the substrate surface. These unusual kinetic processes lead to some new growth features such as growth instability (e.g., increased slope of rim walls) and asymmetrical slope of the inner and outer sidewalls of the crater rims.

CONCLUSIONS

We have shown that the reduction of Cu_2O islands on Cu(100) surfaces results in the growth of the reduced phase on the substrate surface surrounding the reducing oxide islands rather than on the parent oxide, which is fundamentally different from the reduction of bulk oxides. The kinetic data on the size evolution of reducing oxide islands agree well with a perimeter dissociation model. The reduction of these surface oxide islands leads to the formation of surface craters and the growth of the crater rim is controlled by homoepitaxial growth of Cu adatoms dislodged from the reducing Cu_2O islands. These types of *in situ* investigations provide unique understanding in phase transitions and phase stabilities of surface oxide nanostructures. Since oxide island formation during oxidation has been observed in many other metals systems including Ni, Fe, Ti, Co, Pd, Ir, Sn, as well as in Cu, we expect such processes to be easily feasible in many metal systems by carefully choosing oxidation-reduction conditions.

REFERENCES

1 B. Delmon, in *Handbook of Heterogeneous Catalysis*, edited by G. Ertl, Knozinger, H., Weitkamp, J. (Wiley-VCH, New York, 1997), p. 264.
2 J. Li, J. W. Mayer, and K. N. Tu, Phys. Rev. B **45**, 5683 (1992).
3 H. H. Kung, *Transition Metal Oxides: Surface Chemistry and Catalysis* (Elsevier, New York, 1989).
4 J. A. Rodriguez, J. C. Hanson, A. I. Frenkel, J. Y. Kim, and M. Perez, J. Am. Chem. Soc. **124**, 346 (2002).
5 J. Y. Kim, J. A. Rodriguez, J. C. Hanson, A. I. Frenkel, and P. L. Lee, J. Am. Chem. Soc. **125**, 10684 (2003).
6 R. P. Furstenau, G. Mcdougall, and M. A. Langell, Surface Science **150**, 55 (1985).
7 M. L. McDonald, J. M. Gibson, and F. C. Unterwald, Rev. Sci. Instrum. **60**, 700 (1989).
8 G. W. Zhou and J. C. Yang, Phys. Rev. Lett. **93**, 226101 (2004).
9 G. W. Zhou and J. C. Yang, Applied Surface Science **210**, 165 (2003).
10 G. W. Zhou and J. C. Yang, Phys. Rev. Lett. **89**, 106101 (2002).
11 M. Hansen, *Constitution of Binary Alloys* (McGraw-Hill, NY, 1958).
12 F. Buatier de Mongeot, W. G. Zhu, A. Molle, R. Buzio, C. Boragno, U. Valbusa, E. G. Wang, and Z. Y. Zhang, Phys. Rev. Lett. **91**, 016102 (2003).
13 P. Smilauer and D. D. Vvedensky, Phys. Rev. B **52**, 14263 (1995).
14 G. Boisvert and L. J. Lewis, Phys. Rev. B **56**, 7643 (1997).
15 W. G. Zhu, F. Buatier de Mongeot, U. Valbusa, E. G. Wang, and Z. Y. Zhang, Phys. Rev. Lett. **92**, 106102 (2004).
16 J.-K. Zuo and J. F. Wendelken, Phys. Rev. Lett. **78**, 2791 (1997).
17 S. C. Wang and G. Ehrlich, Phys. Rev. Lett. **70**, 41 (1993).
18 J. G. Amar and F. Family, Phys. Rev. Lett. **77**, 4584 (1996).
19 G. Ehrlich and F. Hudda, J. Chem. Phys. **44**, 1039 (1966).
20 R. L. Schwoebel and E. J. Shipsey, Journal of Applied Physics **37**, 3682 (1966).
21 M. C. Bartelt and J. W. Evans, Phys. Rev. Lett. **75**, 4250 (1995).
22 J. W. Evans, P. A. Thiel, and M. C. Bartelt, Surface Science Reports **61**, 1 (2006).